Prabha Materials Science Letters
Vol. 5, No. 2, 486-501, 2026
https://doi.org/10.33889/PMSL.2026.5.2.026

Waste Bovid (Buffalo & Goat) Bone-Derived H_3PO_4-Activated Porous Carbon for Supercapacitor Electrode Applications

Bhumi Raj Sharma
Central Department of Physics,
Institute of Science and Technology, Tribhuvan University, Kirtipur, Kathmandu, Nepal.
E-mail: bhysics@gmail.com, bhumi.795711@iost.tu.edu.np

D. Parajuli
Research Centre for Applied Science and Technology,
Tribhuvan University, Kirtipur, Nepal.
&
Student Welfare and Sports Directorate,
Tribhuvan University, Kirtipur, 44613, Kathmandu, Nepal.
Corresponding author: deepenparaj@gmail.com, deependra.parajuli@trc.tu.edu.np

Nunu Lal Sahu
Central Department of Physics,
Institute of Science and Technology, Tribhuvan University, Kirtipur, Kathmandu, Nepal.
&
Department of Physics
Tri-Chandra Multiple Campus (Tribhuvan University), Ghantaghar, Kathmandu, Nepal.
E-mail: nunulalshah999@gmail.com, nunu.shah@trc.tu.edu.np

Amar Prasad Yadav
Central Department of Chemistry,
Tribhuvan University, Kathmandu, Nepal.
E-mail: amar2@yahoo.com, amar.yadav@cdc.tu.edu.np

Dipak Kumar Gupta
Central Department of Chemistry,
Tribhuvan University, Kirtipur, Kathmandu, Nepal.
E-mail: deepakguptas2012@yahoo.com, deepak.gupta@cdc.tu.edu.np

Armila Nyachhyon Rajbhandari
Central Department of Chemistry,
Tribhuvan University, Kathmandu, Nepal.
E-mail: armila3@yahoo.com, armila.rajbhandari@cdc.tu.edu.np

(Received on April 21, 2026; Revised on July 4, 2026 & July 22, 2026 & July 23, 2026; Accepted on July 29, 2026)

Abstract

Porous activated carbon derived from waste buffalo and goat bones was explored for aqueous supercapacitor electrodes using H_3PO_4 as an activating chemical. Among several prepared samples with impregnation ratios 1:1 – 1:3 and carbonization from 400 °C to 600 °C, buffalo bone-derived carbon (BBAC-2-500) exhibited a higher specific surface area of 1724 $m^2\ g^{-1}$. Goat bone-derived carbon (GBAC-3-600) showed a surface area of 1119 $m^2\ g^{-1}$. Raman analysis found slightly higher defect density, and FTIR revealed a greater amount of oxygen bonding functional groups in BBAC-2-500. XRD confirmed that both materials were amorphous, with a minor structural ordering in GBAC-3-600. BBAC-2-500 delivered a specific capacitance of 280 $F\ g^{-1}$ in 6 M KOH electrolyte at 1 $A\ g^{-1}$ and an energy density (ED) of 14 $Wh\ kg^{-1}$ at a power density (PD) of 300 $W\ kg^{-1}$. GBAC-3-600 achieved

236 F g^{-1} and 11.8 Wh kg^{-1} under the same conditions. The BBAC-2-500 electrode retained 96.87% capacitance after 10,000 cycles and 99.11% coulombic efficiency. These findings demonstrate that the combined effects of precursor selection and activation conditions govern the electrochemical performance of bone-derived carbon electrodes.

Keywords- Buffalo/Goat Bone, Waste biomass, Nanoporous carbon, Energy storage, Electrode materials.

1. Introduction

The rapid production of energy to meet increasing demands requires storing excess energy and then using it. Conventional batteries, however, are not only large in size and heavy in weight but also relatively harmful and high-cost sources of energy (Larcher & Tarascon, 2015). Because of the sharp decline in performance, low durability, and limited specific power, despite their high-specific energy, electric vehicles and portable devices demand alternative power resources such as supercapacitors (Iqbal et al., 2020). But even a fully charged supercapacitor (SC) delivers small specific energy, which constrains large-scale commercialization of supercapacitors. Supercapacitors (SCs) have comparatively lower energy density (ED) but higher power density (PD) and longer charging-discharging cycles (Kötz & Carlen, 2000). Increasing capacitance increases specific energy because it depends on the capacitance as well as the square of the voltage. In this context, activated carbon (AC) is widely used for SC based on its high specific surface area (SSA), cost-effectiveness, and eco-friendly nature (Yassine & Fabris, 2017). However, the common sources of AC such as coal, petroleum, and their derivatives cause environmental pollution. Therefore, attention has shifted toward low-cost and eco-friendly alternatives with high carbon yield, such as waste biomass (Chu et al., 2016). Utilizing animal and plant waste improves resource use and reduces environmental impact. Traditionally, bone waste has been dumped as biomass waste such as buffalo, goat, and cow bones can be processed into activated carbon for SC applications at low cost. This approach also helps in reducing unmanaged waste in local communities, making it highly practical and environmentally responsible.

The ability of SCs is particularly dependent on electrode materials. In EDLCs, the high surface area of electrodes and nanometer-scale ion separation enable large charge accumulation without redox reactions, leading to long cycle life (Wang et al., 2016b). For efficient operation, the electrode material should possess high SSA, good electrical conductivity, and a well-distributed pores. The pore size compatible with the ion size, i.e., less than 1nm, has maximum contribution to capacitance (Simon & Gogotsi, 2008). This highlights why tuning pore size is a significant step in preparing high-performance electrode materials.

Activation of carbon is essential for better performance (Neme et al., 2022). It can be activated chemically and physically. KOH, NaOH, H_3PO_4, or $ZnCl_2$ can be used for chemical activation, while carbon dioxide gas and steam can be used for physical activation (Marsh & Rodríguez-Reinoso, 2006). Animal bones are good precursors for AC because they are rich in carbon and calcium phosphate, but contain high ash content, primarily composed of hydroxyapatite, which can hinder micropore development (Hart et al., 2022; Nwankwo et al., 2018). Acid or alkali activation addresses this limitation. The presence of residual inorganic compounds plays a significant role based on the intended application. In adsorption processes, these residues can obstruct pore development, thereby reducing adsorption efficiency (Nwankwo et al., 2018). However, in supercapacitor applications, they may contribute to enhanced pseudocapacitive behavior. For example, nitrogen-doped carbon synthesized from pork, eel, and blackfish bones exhibited specific capacitances of 263–302 F/g in 6 M KOH electrolyte. This performance was attributed to microporosity and heteroatom doping (Niu et al., 2019). Similarly, pyrolyzed tuna head bone carbon achieved 417 F/g with an energy density of 11.8 Wh/kg (Wulandari et al., 2024). This shows why process variables such as the activating agent and activation temperature control electrochemical performance.

This work reports a simple and low-cost H_3PO_4 activation to synthesize activated carbons from buffalo and goat bones for supercapacitor applications. Phosphoric acid is milder, safer, and scalable than KOH or $ZnCl_2$ (Luo et al., 2019). In addition, it introduces phosphorus functionalities, expands the carbon skeleton, and generates well-developed micro–mesoporous structures (Ahmadpour & Do, 1996; Benaddi et al., 1998; Luo et al., 2019). Further, buffalo and goat bones are common household, restaurant, and slaughterhouse wastes in Nepal. Therefore, these bone wastes are abundant precursors for circular bioeconomy-based carbon materials. Although numerous synthesized carbons have been studied for supercapacitor applications, most of the investigations have worked on plant biomass. Comparative studies on buffalo and goat bones under identical activation conditions remain scarce. Furthermore, the influence of these precursors on pore development and electrochemical behavior is insufficient. This represents an important research gap. Therefore, a comparative investigation of waste buffalo- and goat-bone-derived carbons can help to understand the roles of the precursor and activation conditions on porous architecture and charge-storage performance.

2. Materials and Methods

2.1 Material Synthesis

Waste buffalo bones and castrated male goat rib bones were collected from local meat market in Pokhara, Nepal. The bones were thoroughly cleaned to remove attached meat and fat and then boiled for 2 hours to wash residual organics. The bones were dried at 60 °C for 24 hrs. These dried bones were grounded in a domestic kitchen grinder for 3 minutes.

The bone powder was activated at different weight ratios of 1:1, 1:2, and 1:3 of bone and H_3PO_4. The appropriate amount of H_3PO_4 was mixed with 2.5 g of bone and stirred in 10 mL of deionized water. The mixture was sonicated for 30 minutes, impregnated for 10 hours, and then dried at 100 °C for 12 hours.

Figure 1. Schematic representation of bone carbon synthesis from bone waste.

The dried samples were carbonized under a nitrogen environment at temperatures of 400 °C to 600 °C for 2 hrs with a heating rate of 5 °C/min. H_3PO_4 cannot completely dry up and crosslink the precursors below

400 °C, whereas above 600 °C it can etch and collapse micropores. The carbonized materials were cleaned with HCl and distilled water. It was continued until a neutral pH value was obtained, which is then dried at 60 °C for 24 hrs. The final samples were labeled as BBAC-2-500 representing buffalo bone activated at a 1:2 ratio and carbonized at 500 °C and GBAC-3-600 representing goat bone activated at 1:3 ratio and carbonized at 600 °C. **Figure 1** shows a schematic demonstration of this work.

2.2 Physiochemical Characterization

The morphology was scanned by scanning electron microscope (JEOL JSM-IT300 SEM). N_2 adsorption–desorption isotherms were obtained at 77 K via a Micromeritics ASAP 2020 analyzer. The materials were degassed for 12 h at 200 °C under high vacuum. The Brunauer-Emmett-Teller (BET) method was employed to determine SSA.

Raman spectroscopy using a Renishaw in Via micro-Raman spectrometer with a 532 nm excitation laser was employed to study defect density, graphitic ordering, and bond-structure. The D, G, and 2D bands were fitted to determine I_D/I_G ratios. Fourier Transform Infrared (FTIR) spectra were recorded using an IR Affinity-1S in the range 4000–400 cm^{-1}. The XRD Bruker D_2 Phaser utilized Cu Kα radiation (λ = 0.15406 nm) at 30 kV and 10 mA to analyze structural phases and the degree of ordering. Patterns were collected over a 2θ range of 10 to 80° with a step size of 0.02°.

2.3 Electrochemical Measurement

The carbon was investigated using a CHI660E electrochemical workstation. The active carbon was mixed with conductive carbon and PVDF at a mass ratio of 8:1:1. N-methyl-2-pyrrolidone (NMP) was used to make uniform ink. The paste was sonicated for 30 minutes. After coating onto nickel foam of size 1.0 × 1.0 cm^2, the foams were dried at 60 °C for 12 hours. The mass was recorded before coating and after drying the foam.

A three-electrode arrangement in 6 M KOH electrolyte was used by connecting platinum metal for counter electrode and a saturated calomel electrode (SCE) for reference electrode. Cyclic voltammetry (CV) at scan rates of 5 mV/s to 200 mV/s and galvanostatic charge-discharge (GCD) profiles between 1 A/g and 4 A/g were recorded. EIS was performed in the frequency range of 100 kHz to 1 Hz using a sinusoidal perturbation of 5 mV.

3. Result and Discussion

3.1 Functional Group Evolution

The FTIR spectra of BBAC-2-500 and GBAC-3-600 are shown in **Figure 2**. A broad band near 3489 cm^{-1} signals O–H stretching vibrations. The band near 2730 cm^{-1} is caused by C–H stretching vibrations, the weak band around 2307 cm^{-1} is related to C–N/C–C vibrations, the strong band at approximately 1628 cm^{-1} hints the overlapping C=O and aromatic C=C stretching vibrations. The band at around 1140 cm^{-1} is due to C–O stretching vibrations. The band near 699 cm^{-1} is linked with C–H out-of-plane bending vibrations. Both samples show similar and oxygen-containing functional groups. However, the differences in the intensity of the O–H, C=O/C=C, and C–O bands suggest variations in the quantity. As these functional groups can enhance the wettability of the carbon surface and facilitate electrolyte ion transport, the presence of more oxygenated functional groups in BBAC-2-500 can improve electrochemical performance as well.

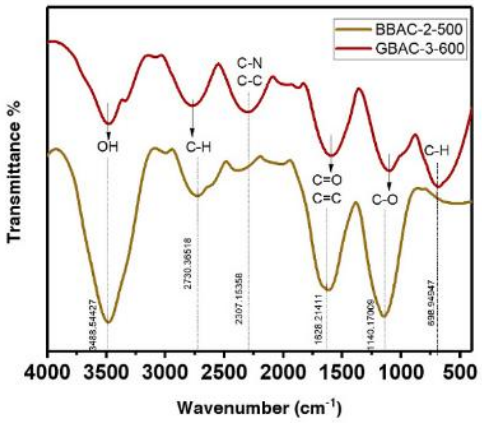

Figure 2. FTIR spectra of BBAC-2-500 (olive gold line) and GBAC-3-600 (red line).

3.2 XRD Analysis of Crystalline Structure

Figure 3 shows the structural characteristics (XRD) of the activated carbons. Two broad diffraction peaks typical of turbostratic carbon are observed. A broad (002) reflection at 23–25° and a weaker (100)/(101) reflection near 43–44° indicate amorphous carbon with limited structural ordering (Chae & Chen, 2014). Such carbon framework provides enough accessible sites for charge storage and facilitates electrolyte ion access (Hu et al., 2014). BBAC-2-500 exhibits a broader and less intense (002) peak centered at approximately 23.5° and GBAC-3-600 shows a slightly narrower (002) peak at a higher angle around 24.8°.

BBAC-2-500 displays faint sign or absence of calcium phosphate phases, while GBAC-3-600 shows weak diffraction peaks of β-tricalcium phosphate. The higher impregnation ratio of H_3PO_4 enhances the formation of amorphous phosphate species. Conversely, the slightly higher activation temperature increases the crystallinity of the remaining phosphate species. Therefore, the observed diffraction peaks are possibly the cause of acid-induced mineral dissolution and thermally driven structural ordering of the residual calcium phosphate (Wang & Nancollas, 2008).

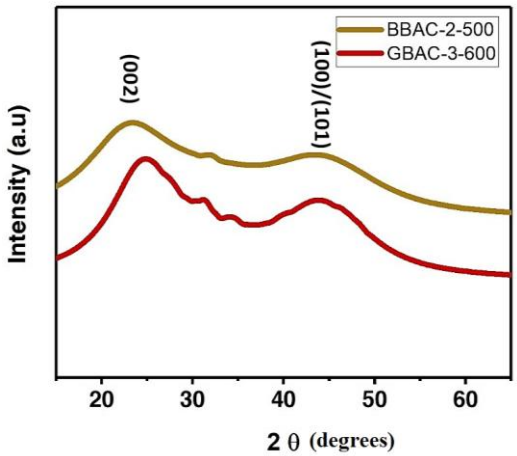

Figure 3. X-ray Diffraction patterns BBAC-2-500 (olive gold line) and GBAC-3-600 (red line).

3.3 Structural Ordering and Defects

Figure 4 displays the Raman spectra, the D band of BBAC-2-500 appears at nearly 1354.5 cm^{-1} and the G band is at about 1577.0 cm^{-1}. These bands indicate distorted sp^2 carbon networks. The broad 2D band centered near 2689.5 cm^{-1} is an indicator of turbostratic carbon with limited structural ordering. The ID/IG ratio difference 0.02 indicates a small increase in defect density in BBAC-2-500 compared to GBAC-3-600. The D band (~1350 cm^{-1}) is from orderless structure and carbon and G (~1580 cm^{-1}) is from vibration of sp^2 graphitic carbons in same plane (Li et al., 2018).

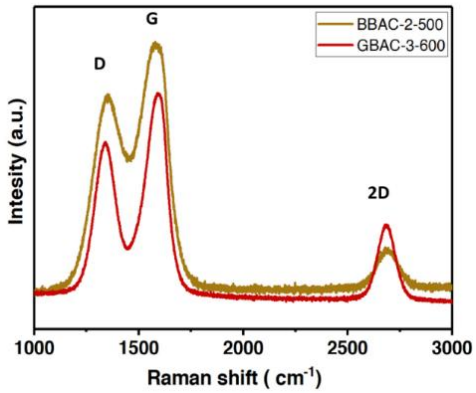

Figure 4. Raman Spectra of BBAC-2-500 (olive gold line) and GBAC-3-600 (red line).

GBAC-3-600 exhibits a D band at approximately 1340.5 cm^{-1} and relatively sharper G band at about 1586.0 cm^{-1}. The lower I_D/I_G ratio of 0.96 suggests a modest increase in local structural ordering. The comparatively sharper 2D band observed near 2684.5 cm^{-1} also indicates modestly higher local structural ordering and largely a turbostratic carbon structure. It suggests slight increase in local structural ordering, which is consistent with the slightly lower I_D/I_G ratio along with sharper G and 2D bands in Raman spectra. (Cançado et al., 2008; Schuepfer et al., 2020).

3.4 Morphology Analysis Through SEM Imaging

Figure 5(a–c) and **5(d–f)** show SEM micrographs of GBAC-3-600 and BBAC-2-500, respectively, at low and high magnifications. The GBAC-3-600 sample reveals an open framework with irregularly shaped pores ranging from tens to a few hundred nanometers. This architecture may result from the decomposition of the collagen-rich bone at the higher temperature combined with the higher H_3PO_4 impregnation ratio. This can generate gaseous products that create interconnected voids (Benaddi et al., 1998; Luo et al., 2019). A greater etching impact of the activating chemical is indicated by the thinner pore walls and less organized texture. Organic and mineral phases may be removed during the activation process when the concentration of acid is increased.

The BBAC-2-500 sample shows a relatively compact morphology with a well-connected network of larger pores. Although micropores cannot be directly resolved by SEM, N_2 adsorption-desorption isotherms shows substantial micropores filling. The moderate acid ratio and lower pyrolysis temperature favor the preservation of a denser carbon framework (Zhang et al., 2023). The resulting sponge-like appearance with uniform pore distribution reflects effective pore development through phosphoric acid activation. The release of volatiles during carbonization assists in opening channels within the mineral-rich precursor (Benaddi et al., 1998; Luo et al., 2019).

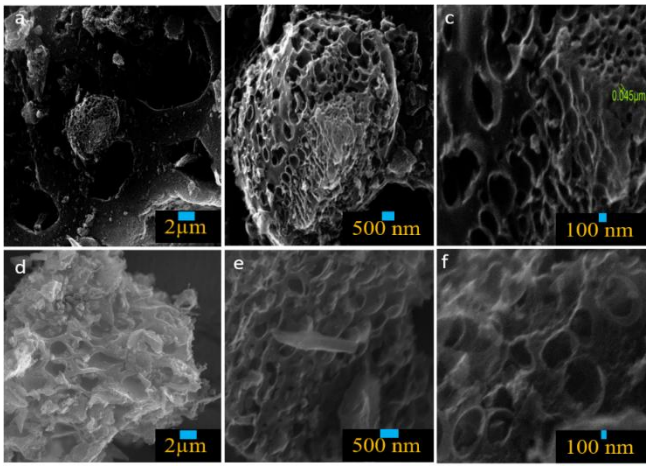

Figure 5. (a–c) SEM images of GBAC-3-600 at low to high magnifications, with scale bars of 2 µm, 500 nm, and 100 nm, respectively. (d–f) SEM images of BBAC-2-500 at low to high magnifications, with scale bars of 2 µm, 500 nm, and 100 nm, respectively.

3.5 Surface Area and Pore Structure

Figure 6(a-c) displays the nitrogen adsorption–desorption isotherms measured at 77 K. The samples were degassed at 200 °C for 12 h under high vacuum. **Table 1** summarizes the textural characteristics obtained from nitrogen adsorption analysis.

Micropore filling is indicated by BBAC-2-500's Type I(b) isotherm as shown in **Figure 6(a)** where BBAC-2-500 (adsorption) is olive gold line and BBAC-2-500 (desorption) is red line. It shows a steep uptake at a very low relative pressure. A small hysteresis loop at higher P/P_0 indicates the presence of narrow mesopores, while the adsorption branch approaches a plateau at higher P/P_0 (Ello et al., 2013; Monson, 2012). The high surface area of 1723.8 $m^2\ g^{-1}$ and monolayer adsorption volume of 396.05 $cm^3\ g^{-1}$ are in agreement with the large accessible internal surface indicated by the Type I(b) isotherm. The average pore width is 2.34 ± 0.20 nm and the total pore volume is 1.0104 ± 0.0101 $cm^3\ g^{-1}$ at $P/P_0 = 0.95$. These results support a micro-mesoporous pore structure, which is common in H_3PO_4-activated bone-derived carbons. This micro-mesoporous structure provides a high accessible surface area and ion transport pathways. The larger SSA and micro-mesoporous structure of buffalo bone-derived carbon enhanced its electrochemical performance (Li et al., 2021; Sayed et al., 2024).

The adsorption line with blue and desorption line with purple, for GBAC-3-600, shown in **Figure 6(b)**. It has a Type IV(a) isotherm with a prominent H2(b) hysteresis loop that extends from mid to high relative pressures. This suggests a structure dominated by mesopores with constricted pore necks and irregular pore shape. The smaller BET surface area of 1119 $m^2\ g^{-1}$ and monolayer adsorption volume 257.10 $cm^3\ g^{-1}$ STP (at Standard Temperature and Pressure), compared with BBAC-2-500, shows a lower accessible internal surface. A wider pore network that is advantageous for ion transport is indicated by the greater average pore diameter of 3.50 ± 0.06 nm and overall pore volume 0.9784 ± 0.0098 $cm^3\ g^{-1}$. Mesoporosity dominates the overall adsorption behavior. However, there is still a slight low-pressure uptake that is characteristic of H_3PO_4 activation and indicates persistent micropores (Kwiatkowski & Broniek, 2021; Zhu et al., 2021).

The BET fitting ranges (P/P_0 = 0.05-0.20 for BBAC-2-500 and 0.05-0.30 for GBAC-3-600) were chosen because they are mostly used for mixed micro-/mesoporous carbons. The relatively high uncertainty

associated with the obtained C-constant for BBAC-2-500 (86.4 ± 43.2) can be the effect of the stronger adsorption and the limited pressure range available for monolayer formation. In contrast, GBAC-3-600 exhibits a more uniform adsorption behavior and lower C-constant variability (80.9 ± 19.9), consistent with its mesopore-dominated architecture. The reliability of the derived parameters is supported by the isotherm shapes, consistency of the BET fit ($R^2 > 0.998$ for both materials), and the agreement with pore-volume analysis and electrochemical results.

Figure 6(c) shows the comparison of the adsorption and desorption patterns of both samples.

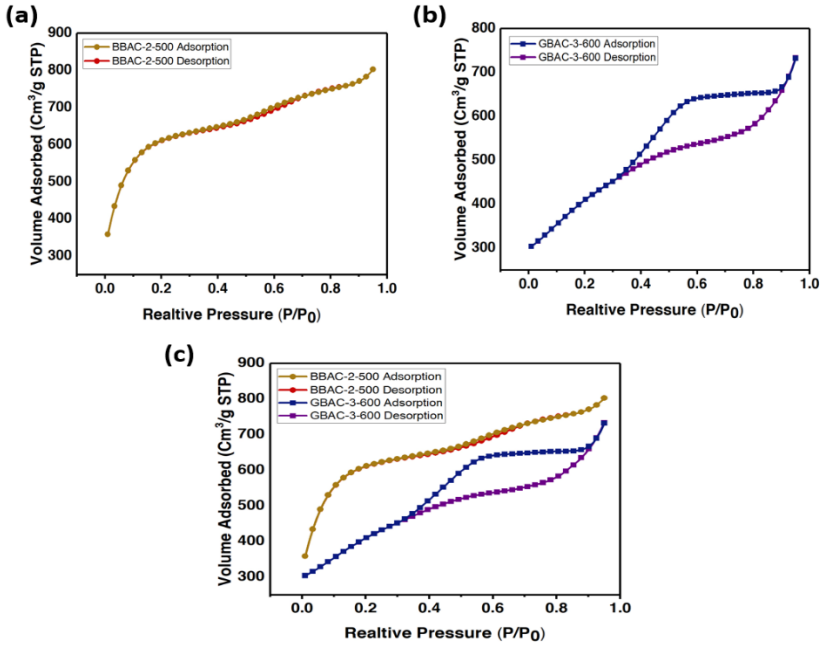

Figure 6. (a-c) N2 adsorption-desorption isotherms of BBAC-2-500 (olive gold line) and GBAC-3-600 (red line), and combined isotherms of both samples.

Table 1. Textural values of the samples obtained from BET analysis.

Sample	BET SSA ($m^2\ g^{-1}$)	Monolayer volume Vm ($cm^3\ g^{-1}$ STP)	Total pore volume at P/P_o = 0.95 ($cm^3\ g^{-1}$)	Average pore diameter (nm)	BET C-constant	R^2 (BET fit)
BBAC-2-500	1723.8 ± 145.3	396.05 ± 33.39	1.0104 ± 0.0101	2.34 ± 0.20	86.4 ± 43.2	0.99804
GBAC-3-600	1119.0 ± 139.0	257.10 ± 3.19	0.9784 ± 0.0098	3.50 ± 0.06	80.9 ± 19.9	0.99951

The SSA values obtained in this work are comparable with previously reported animal bone-derived carbons such as cooked chicken, cattle, pig, and fish bones with specific surface area 2235.8$m^2\ g^{-1}$, 2096 m^2/g^{-1}, 2157 $m^2\ g^{-1}$, and ranging from 1160–1260 $m^2\ g^{-1}$ respectively (Niu et al., 2019; Tarimo et al., 2022, Niu et al., 2017).

3.6 Electrochemical Characterization

Figure 7(a) and **7(c)** show the CV profiles of BBAC-2-500 and GBAC-3-600 respectively, at scan rates of 5 mV s^{-1} (blue line), 50mV s^{-1} (purple line), to 200 mV s^{-1} (brown line) across Saturated Calomel Electrode

(SCE) (Calomel is mercury chloride and saturated calomel electrode consists of mercury chloride and saturated potassium chloride). The CV shape even at higher scan rates indicates that both materials maintain rapid ion mobility. The GCD curves for BBAC-2-500 and GBAC-3-600 are shown in **Figure 7(b, d)**. The nearly symmetric triangular curves are a clear sign of reversibility during charge-discharge cycles and limited faradaic reaction involvement.

The brown, blue, purple and green line in **Figure 7(b)** and **7(d)** represent the GCD curves with current density of 1 Ag^{-1}, 2 Ag^{-1}, 3 Ag^{-1}, 4 Ag^{-1} for BBAC-2-500 and 1 Ag^{-1}, 1.3 Ag^{-1}, 2 Ag^{-1}, 2.7 Ag^{-1} for GBAC-3-600 respectively.

Figure 8(a–f) displays comparative electrochemical evaluation of BBAC-2-500 (red line) and GBAC-3-600 (blue line). The CV curves at 5 mV s^{-1} shown in **Figure 8(a)** reveal that both electrodes retain quasi-rectangular shapes. However, BBAC-2-500 delivers a higher current density response compared to GBAC-3-600. At a scan rate of 50 mV s^{-1}, the difference between the two electrodes becomes more pronounced as illustrated in **Figure 8(c)**. BBAC-2-500 exhibits longer discharge times at 1 A g^{-1} compared to GBAC-3-600 as shown in **Figure 8(b)**. At 2 A g^{-1}, the triangular GCD profile of GBAC-3-600 shows reduced discharge time and increased IR drop (**Figure 8(d)**). The specific capacitance vs. scan rate and current density are shown in **Figures 8(e)** and **8(f)** respectively. At 5 mV s^{-1}, BBAC-2-500 achieved a specific capacitance of 388 F g^{-1} and GBAC-3-600 recorded 317 F g^{-1}. As the scan rate was increased to 200 mV s^{-1}, both electrodes' capacitance was decreased due to limited ion diffusion. BBAC-2-500 consistently outperformed GBAC-3-600.as shown in **Figure 8(f)**, BBAC-2-500 specific capacitance reached up to 280.49 F g^{-1} at a current density of 1 A g^{-1}, and GBAC-3-600 recorded 236.3 F g^{-1}. BBAC-2-500 performed better than the goat bone-derived sample at 2 A g^{-1} as well, where BBAC-2-500 and GBAC-3-600 delivered 97.1 F g^{-1} and 68.91 F g^{-1}, respectively. The capacitance at high current densities suggests that BBAC-2-500 supports faster ion diffusion through its interconnected micro–mesopore channels.

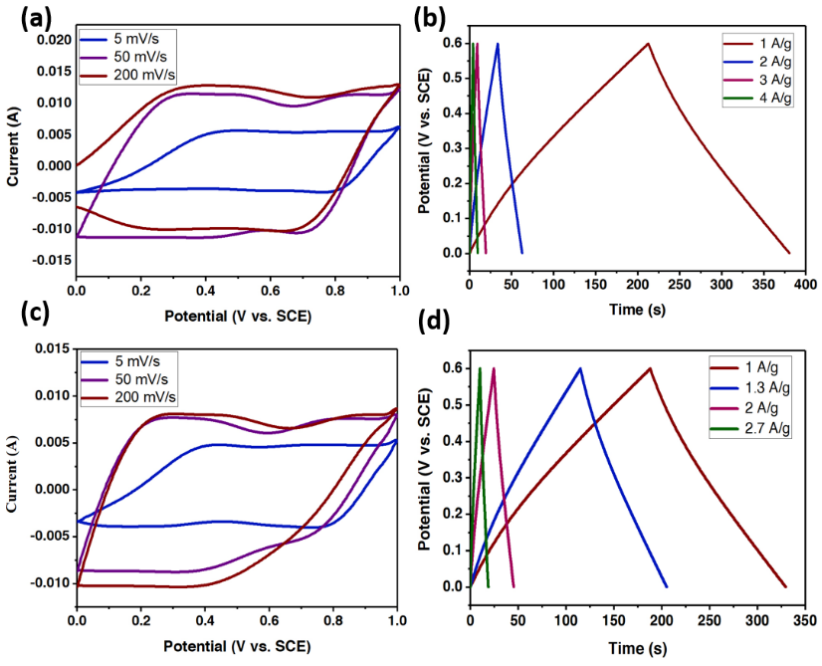

Figure 7. (a, c) CV curves of BBAC-2-500 and GBAC-3-600 at scan rates 5 mV s^{-1}, 50 mV s^{-1}, and 200 mV s^{-1}, respectively, and (b, d) GCD profiles of BBAC-2-500 and GBAC-3-600 at 1 A g^{-1} to 4 A g^{-1}.

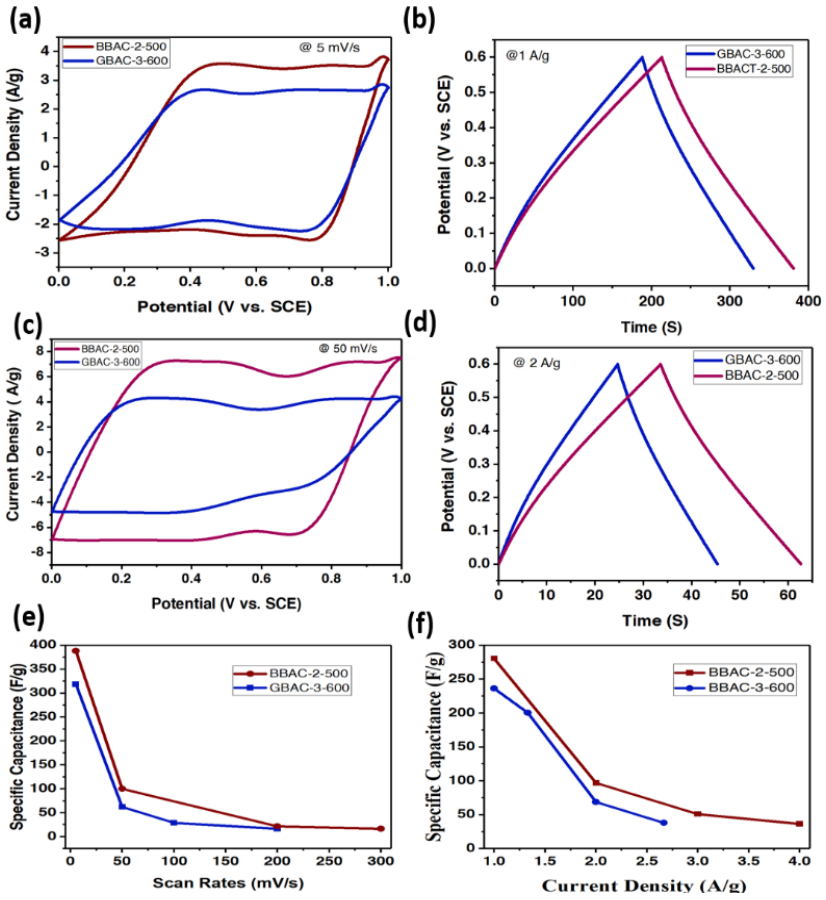

Figure 8. (a, c) CV curves of both BBAC-2-500 and GBAC-3-600 at a scan rate of 5 mV s^{-1} and 50 mV s^{-1} in 6 M KOH electrolyte respectively, (b, d) GCD curves of BBAC-2-500 and GBAC-3-600 at 1 A g^{-1} and 2 A g^{-1} respectively, and (e, f) Specific capacitance vs. scan rate and current density of BBAC-2-500 and GBAC-3-600, respectively.

In addition to CV and GCD analyses, EIS was carried out to examine the ion transport and resistive characteristics of BBAC-2-500 and GBAC-3-600 electrodes. The Nyquist plots for BBAC-2-500 (red) and GBAC-3-600 (green) are presented in **Figure 9(a)**. Both electrodes exhibit a diminished semicircle in the high-frequency region and a steeply inclined tail in the low-frequency region. The equivalent circuit Rs–(Rct|CPE)–W–CPE was used to fit the experimental data, as shown in **Figure 9(a-i)**. The fitted values are summarized in **Table 2**. BBAC-2-500 exhibits a slightly higher solution resistance (Rs = 3.64 Ω) than GBAC-3-600 (Rs = 1.96 Ω). However, BBAC-2-500 shows a lower charge-transfer resistance (Rct = 0.93 Ω) than GBAC-3-600 (Rct = 1.19 Ω), indicating more efficient interfacial charge transfer. In addition, the steeper low-frequency line of BBAC-2-500 suggests reduced Warburg impedance and improved ion transport kinetics.

Table 2. Equivalent circuit fitting parameters obtained from electrochemical impedance spectroscopy (EIS) analysis.

Sample	Rs (Ω)	Rct (Ω)	CPE exponent (n)
BBAC-2-500	3.64	0.93	0.95
GBAC-3-600	1.96	1.19	0.91

The Ragone plot shown in **Figure 9(b)** illustrates the relationship of energy and power densities of BBAC-2-500 (red) and GBAC-3-600 (blue). BBAC-2-500 delivers a higher specific energy, 14 Wh kg^{-1} at a power output of 300 W kg^{-1}, exhibiting 4.8 Wh kg^{-1} at 600 W kg^{-1}, and then falling to 1.7 Wh kg^{-1} at 1200 W kg^{-1}. GBAC-3-600 exhibits somewhat lower energy values, delivering 11.8 Wh kg^{-1} at 300 W kg^{-1}, 3.4 Wh kg^{-1} at 600 W kg^{-1}, and 1.8 Wh kg^{-1} at 800 W kg^{-1}.

The long-term stability was estimated by 10,000 cycles of GCD cycling at 5 A g^{-1}, as shown in **Figure 9(c)**. BBAC-2-500 retained 96.87% capacitance (blue) with a coulombic efficiency (dark red) of 99.11%, whereas GBAC-3-600 retained 95.78% (gold) with a coulombic efficiency (red) of 98.61%. The high capacitance retention and coulombic efficiency demonstrate the good reversibility and electrochemical stability. The better cycling performance of BBAC-2-500 may be due to the pore structure and larger specific surface area. The GCD profiles at 1A g^{-1} before and after cycling for BBAC -2-500 (red and gold) and GBAC-3-600 (blue and green) respectively, shown in **Figure 9(d)**, exhibit only minor changes in charge-discharge duration and internal resistance drop.

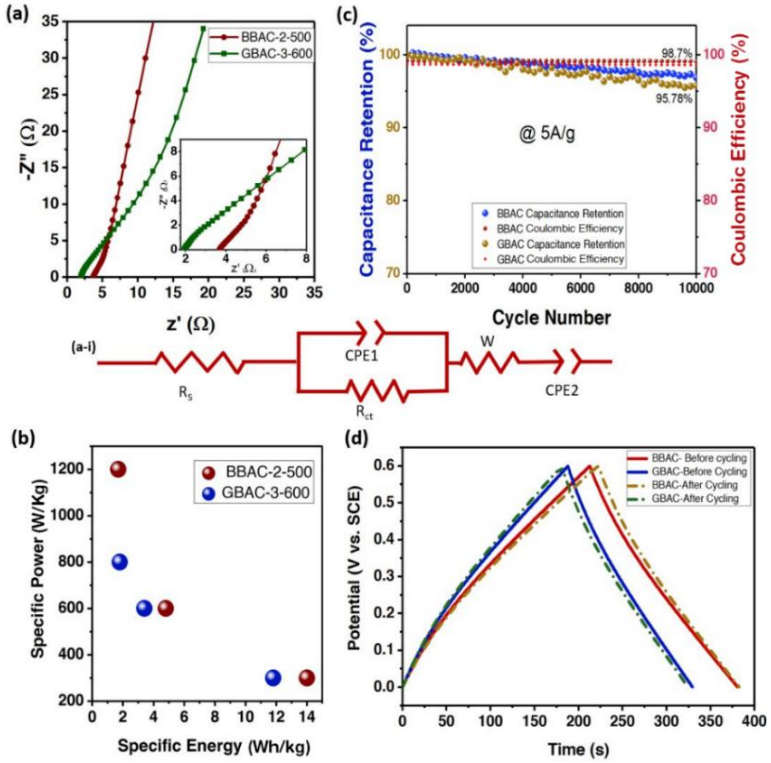

Figure 9. (a) Nyquist plots of BBAC-2-500 and GBAC-3-600 electrodes obtained from EIS ranging from 100 kHz to 1 Hz. (a-i) shows the equivalent circuit model, Rs(CPE1‖Rct)WCPE2. (b) Ragone plot comparing the energy density and power density of BBAC-2-500 and GBAC-3-600 electrodes. (c) Cycling stability and coulombic efficiency measured at 5 A g^{-1} for 10,000 charge–discharge cycles. (d) GCD profiles before and after 10,000 cycles at 1A/g.

The different characterization techniques provide complementary evidence for structural and electrochemical differences. The higher specific capacitance of 280 F g^{-1} of BBAC-2-500 is supported by the larger specific surface area of 1723.8 m^2 g^{-1} and Type I(b) adsorption behavior, indicating substantial micropore filling. On the other hand, GBAC-3-600 shows a lower SSA (1119.0 m^2 g^{-1}), a larger average

pore diameter (3.50 nm), and Type IV(a) adsorption isotherm. These features indicate a more open mesopore-rich pore network that facilitates electrolyte ion transport. Although BBAC-2-500 possesses a substantially higher surface area, the increase in capacitance is not proportional to the increase in SSA. This suggests that not all of the internal surfaces contribute equally to charge storage. In porous carbons, a portion of the surface may be partially accessible to solvated electrolyte ions or located within narrow pore regions. In contrast, GBAC-3-600 benefits from wider mesoporous channels facilitate faster electrolyte ion transport (Sayed et al., 2024). Although GBAC-3-600 possesses a mesopore-rich structure, its energy density decreases more rapidly with increasing power. This is consistent with its lower specific surface area and contribution of mesopores, which provide less surface area for charge storage than micropores.

Overall, the combined analyses demonstrate that the precursor type and activation conditions influence the pore architecture and surface chemistry of biomass-derived carbons. BBAC-2-500 develops a micro-mesoporous pore structure with a slightly higher defect density, a larger specific surface area, and a higher concentration of oxygen-containing functional groups. As a result, it exhibited greater charge storage, higher energy density, lower charge-transfer resistance, and excellent cycling stability. In contrast, GBAC-3-600 exhibits a slightly more ordered carbon structure with a larger average pore size. These findings demonstrate that balancing micro-mesoporous structure for charge storage and efficient ion transport is essential for achieving high-performance bone-derived carbon electrodes (Simon & Gogotsi, 2008).

4. Comparative Analysis

Table 3 compares the electrochemical performance of these samples with other biomass-derived activated carbons. Fish, pork, and bovine bones generally exhibit capacitances, in aqueous electrolytes, ranging from 260 F g^{-1} to 370 F g^{-1} at 0.5 A g^{-1} to 1 A g^{-1} (Mu et al., 2020; L. Niu et al., 2019). BBAC-2-500 developed delivered 280 F g^{-1} at 1 A g^{-1} with an energy density of 14 Wh kg^{-1}, which is comparable to many reported animal bone precursors. GBAC-300-600 showed 236 F g^{-1} at 1 A g^{-1} and 11.8 Wh kg^{-1}, still comparable to reported bone carbons such as pork and eel bone-derived carbons. Therefore, buffalo- and goat bone-derived carbons at the moderate carbonization temperature can achieve promising energy and power densities in aqueous electrolyte supercapacitors.

Table 3. Various biomass-derived carbons' SSA and electrochemical performance are compared with the buffalo and goat bone-derived carbon.

Precursor	SSA m^2/g	Electrolyte	ED (Wh/kg)	PD (W/kg)	Specific Capacitance F/g	Ref. STAM
Fishbone	1137	1 M H_2SO_4	4.8	15	476 at 0.1 A/g	Mu et al. (2020)
		1 M KOH	12.3	50	372 at 0.1 A/g	
Pork bone	1260	6 M KOH	6.5	300	263 at 0.5 A/g	Niu et al. (2019)
Chicken bone	2235.8	1 M $NaNO_3$	17.1	425	0.5 A g^{-1}	Tarimo et al. (2022)
Eel fish bone	1163	6 M KOH	6.8	300	264 at 0.5 A/g	Niu et al. (2019)
Blackfish	1202	6 M KOH	7.0	300	302 at 0.5 A/g	Niu et al. (2019)
Cattle bone	2096	$EMIMB_4$	109.9	4400	258 at 5 A/g	Niu et al. (2017)
Ant Powder	2650	6 M KOH	-	-	576 at 1 A/g	Zhao et al. (2018)
Pig bone	2157	7 M KOH	-	-	185 at .05 A/g	Huang et al. (2011)
Red beetroot	2200	1M Na_2SO_4	-	-	492 at 1 A/g	Selvaraj et al. (2023)
Jute Fiber	1903.48	6 M KOH	-	-	346 at 1 A/g	Manasa et al. (2020)
Coconut shell	1874	2E/Et4NB4	61.2	1500	196 at 1A/g	Sun et al. (2013)
Onion husk	2571	2E/TEABF4	47.5	675	188 at 0.5 A/g	Wang et al. (2016)
Cili fruit	3952.9	$[BMIM]BF_4$	56.6	375	370 at 0.5 A/g	Wu et al. (2024)
Silk	2557	2E/1 M H_2SO_4	9.1	50	264 at 0.1 A/g	Yun et al. (2013)
Buffalo bone	1723.8	6 M KOH	14	300	280 at 1 A/g	This work
Goat bone	1119	6 M KOH	11.8	300	236 at 1 A/g	This work

5. Circular Economy and Sustainability Perspective

Activated porous carbon materials made from waste animal bones support environmental sustainability and the circular economy (Hart et al., 2022). The bone precursors were collected from existing slaughterhouses and deceased animal. This work does not encourage additional animal slaughter or livestock exploitation. Instead, it promotes utilization of unavoidable biological waste that requires disposal. Thus, this work supports a circular bioeconomy (Hart et al., 2022).

6. Conclusion

Bovid bone waste-derived H_3PO_4-activated carbons were evaluated as electrode materials for aqueous supercapacitors. The underlying reasons for superior performance of BBAC-2-500 are the higher specific surface area, the higher abundance of oxygenated functional groups, a slightly higher defect density, and the micro-mesoporous structure characterized by substantial micropore filling.

BBAC-2-500 exhibited a higher specific capacitance (280 F g^{-1} at 1 A g^{-1}) than GBAC-3-600 (236 F g^{-1}), which is consistent with its considerably larger specific surface area (1724.8 vs. 1119.0 m^2 g^{-1}). BBAC-2-500 and GBAC-3-600 achieved energy densities of 14.0 and 11.8 Wh kg^{-1}, respectively, at a power density of 300 W kg^{-1}. Furthermore, BBAC-2-500 retained 96.87% of its initial capacitance after 10,000 cycles with a coulombic efficiency of 99.11%.

This study demonstrates that waste buffalo and goat bones can be used as sustainable precursors. The buffalo-bone-derived carbon exhibited the most balanced combination of micro-mesoporosity, efficient ion transport, and electrochemical performance. Future work should focus on direct precursor compositional analysis and evaluation of two-electrode symmetric supercapacitor devices based on bovid bone-derived carbons.

Conflicts of Interest

The authors declare that they have no known competing financial interests or personal relationships that could have appeared to influence the work reported in this paper.

Acknowledgments

The authors express their gratitude to the University Grants Commission (UGC), Nepal, for research support fund.

AI Disclosure

During the preparation of this work the author(s) used generative AI in order to improve the language of the article. After using this tool/service, the author(s) reviewed and edited the content as needed and take(s) full responsibility for the content of the publication.

References

Ahmadpour, A., & Do, D.D. (1996). The preparation of active carbons from coal by chemical and physical activation. *Carbon*, *34*(4), 471-479. https://doi.org/10.1016/0008-6223(95)00204-9

Benaddi, H., Legras, D., Rouzaud, J.N., & Beguin, F. (1998). Influence of the atmosphere in the chemical activation of wood by phosphoric acid. *Carbon*, *36*(3), 306-309. https://doi.org/10.1016/S0008-6223(98)80123-1

Cançado, L.G., Takai, K., Enoki, T., Endo, M., Kim, Y.A., Mizusaki, H., Speziali, N.L., Jorio, A., & Pimenta, M.A. (2008). Measuring the degree of stacking order in graphite by Raman spectroscopy. *Carbon*, *46*(2), 272-275. https://doi.org/10.1016/j.carbon.2007.11.015

Chae, J.H., & Chen, G.Z. (2014). Influences of ions and temperature on performance of carbon nano -particulates in supercapacitors with neutral aqueous electrolytes. *Particuology*, *15*, 9-17. https://doi.org/10.1016/j.partic.2013.02.008

Chu, S., Cui, Y., & Liu, N. (2016). The path towards sustainable energy. *Nature Materials*, *16*(1), 16-22. https://doi.org/10.1038/nmat4834

Ello, A.S., De Souza, L.K.C., Trokourey, A., & Jaroniec, M. (2013). Coconut shell-based microporous carbons for CO2 capture. *Microporous and Mesoporous Materials*, *180*, 280-283. https://doi.org/10.1016/j.micromeso.2013.07.008

Hart, A., Ebiundu, K., Peretomode, E., Onyeaka, H., Nwabor, O.F., & Obileke, K.C. (2022). Value -added materials recovered from waste bone biomass: technologies and applications. *RSC Advances*, *12*(34), 22302-22330. https://doi.org/10.1039/d2ra03557j

Hu, C., Sedghi, S., Madani, S.H., Silvestre-Albero, A., Sakamoto, H., Kwong, P., Pendleton, P., Smernik, R.J., Rodríguez-Reinoso, F., Kaneko, K., & Biggs, M.J. (2014). Control of the pore size distribution and its spatial homogeneity in particulate activated carbon. *Carbon*, *78*, 113-120. https://doi.org/10.1016/j.carbon.2014.06.054

Huang, W., Zhang, H., Huang, Y., Wang, W., & Wei, S. (2011). Hierarchical porous carbon obtained from animal bone and evaluation in electric double-layer capacitors. *Carbon*, *49*(3), 838-843. https://doi.org/10.1016/j.carbon.2010.10.025

Iqbal, A., Sambyal, P., & Koo, C.M. (2020). 2D MXenes for electromagnetic shielding: a review. *Advanced Functional Materials*, *30*(47), 2000883. https://doi.org/10.1002/ADFM.202000883

Kötz, R., & Carlen, M. (2000). Principles and applications of electrochemical capacitors. *Electrochimica Acta*, *45*(15-16), 2483-2498. https://doi.org/10.1016/S0013-4686(00)00354-6

Kwiatkowski, M., & Broniek, E. (2021). Computer analysis of the porous structure of activated carbons derived from various biomass materials by chemical activation. *Materials*, *14*(15), 4121. https://doi.org/10.3390/MA14154121

Larcher, D., & Tarascon, J.M. (2015). Towards greener and more sustainable batteries for electrical energy storage. *Nature Chemistry*, *7*(1), 19-29. https://doi.org/10.1038/nchem.2085

Li, S., Xing, T., Wang, Y., Lu, P., Kong, W., Li, S., & Wei, X. (2021). Pore structure regulation and electrochemical performance characterization of activated carbon for supercapacitors. *Frontiers in Energy Research*, *9*, 680761. https://doi.org/10.3389/fenrg.2021.680761

Li, X., Liu, Y., Zeng, Z., Wang, P., Fang, Y., & Zhang, L. (2018). Investigation on tip enhanced Raman spectra of graphene. *Spectrochimica Acta Part A: Molecular and Biomolecular Spectroscopy*, *190*, 378-382. https://doi.org/10.1016/j.saa.2017.07.069

Luo, Y., Li, D., Chen, Y., Sun, X., Cao, Q., & Liu, X. (2019). The performance of phosphoric acid in the preparation of activated carbon-containing phosphorus species from rice husk residue. *Journal of Materials Science*, *54*(6), 5008-5021. https://doi.org/10.1007/s10853-018-03220-x

Manasa, P., Lei, Z.J., & Ran, F. (2020). Biomass waste derived low cost activated carbon from carchorus olitorius (jute fiber) as sustainable and novel electrode material. *Journal of Energy Storage*, *30*, 101494. https://doi.org/10.1016/j.est.2020.101494

Marsh, H., & Rodriguez-Reinoso, F. (2006). *Activated carbon*. Elsevier Science Ltd. https://doi.org/10.1016/B978-0-08-044463-5.X5013-4

Monson, P.A. (2012). Understanding adsorption/desorption hysteresis for fluids in mesoporous materials using simple molecular models and classical density functional theory. *Microporous and Mesoporous Materials*, *160*, 47-66. https://doi.org/10.1016/j.micromeso.2012.04.043

Mu, J., Wong, S.I., Li, Q., Zhou, P., Zhou, J., Zhao, Y., Sunarso, J., & Zhuo, S. (2020). Fishbone-derived N-doped hierarchical porous carbon as an electrode material for supercapacitor. *Journal of Alloys and Compounds*, *832*, 154950. https://doi.org/10.1016/j.jallcom.2020.154950

Neme, I., Gonfa, G., & Masi, C. (2022). Activated carbon from biomass precursors using phosphoric acid: a review. *Heliyon*, *8*(12). e11940. https://doi.org/10.1016/j.heliyon.2022.e11940

Niu, J., Shao, R., Liang, J., Dou, M., Li, Z., Huang, Y., & Wang, F. (2017). Biomass-derived mesopore-dominant porous carbons with large specific surface area and high defect density as high performance electrode materials for Li-ion batteries and supercapacitors. *Nano Energy*, *36*, 322-330. https://doi.org/10.1016/j.nanoen.2017.04.042

Niu, L., Shen, C., Yan, L., Zhang, J., Lin, Y., Gong, Y., Li, C., Sun, C.Q., & Xu, S. (2019). Waste bones derived nitrogen–doped carbon with high micropore ratio towards supercapacitor applications. *Journal of Colloid and Interface Science*, *547*, 92-101. https://doi.org/10.1016/j.jcis.2019.03.097

Nwankwo, I.H., Nwaiwu, N.E., & Nwabanne, J.T. (2018). Production and characterization of activated carbon from animal bone. *American Journal of Engineering Research*, *7*(7), 335-341.

Sayed, M.S., Aman, D., Fayed, M.G., Omran, M.M., Zaki, T., & Mohamed, S.G. (2024). Unravelling the role of pore structure of biomass-derived porous carbon in charge storage mechanisms for supercapacitors. *RSC Advances*, *14*(34), 24631-24642. https://doi.org/10.1039/d4ra04681a

Schuepfer, D.B., Badaczewski, F., Guerra-Castro, J.M., Hofmann, D.M., Heiliger, C., Smarsly, B., & Klar, P.J. (2020). Assessing the structural properties of graphitic and non-graphitic carbons by Raman spectroscopy. *Carbon*, *161*, 359-372. https://doi.org/10.1016/j.carbon.2019.12.094

Selvaraj, M., Balamoorthy, E., & Manivasagam, T.G. (2023). Biomass derived nitrogen-doped activated carbon and novel biocompatible gel electrolytes for solid-state supercapacitor applications. *Journal of Energy Storage*, *72*, 108543. https://doi.org/10.1016/j.est.2023.108543

Simon, P., & Gogotsi, Y. (2008). Materials for electrochemical capacitors. *Nature Materials*, *7*(11), 845-854. https://doi.org/10.1038/nmat2297

Sun, L., Tian, C., Li, M., Meng, X., Wang, L., Wang, R., Yin, J., & Fu, H. (2013). From coconut shell to porous graphene-like nanosheets for high-power supercapacitors. *Journal of Materials Chemistry A*, *1*(21), 6462-6470. https://doi.org/10.1039/c3ta10897j

Tarimo, D.J., Oyedotun, K.O., Sylla, N.F., Mirghni, A.A., Ndiaye, N.M., & Manyala, N. (2022). Waste chicken bone-derived porous carbon materials as high performance electrode for supercapacitor applications. *Journal of Energy Storage*, *51*, 104378. https://doi.org/10.1016/j.est.2022.104378

Wang, D., Liu, S., Fang, G., Geng, G., & Ma, J. (2016a). From trash to treasure: direct transformation of onion husks into three-dimensional interconnected porous carbon frameworks for high-performance supercapacitors in organic electrolyte. *Electrochimica Acta*, *216*, 405-411. https://doi.org/10.1016/j.electacta.2016.09.053

Wang, L., & Nancollas, G.H. (2008). Calcium orthophosphates: crystallization and dissolution. *Chemical Reviews*, *108*(11), 4628-4669. https://doi.org/10.1021/cr0782574

Wang, Y., Song, Y., & Xia, Y. (2016b). Electrochemical capacitors: mechanism, materials, systems, characterization and applications. *Chemical Society Reviews*, *45*(21), 5925-5950. https://doi.org/10.1039/c5cs00580a

Wu, Y., Peng, S., Chen, B., Dai, L., Wang, X., Yang, W., Lu, S., & Ruan, Y. (2024). In situ O and N self-doped fruit waste-derived microporous activated carbon for all-solid-state supercapacitors. *Energy & Fuels*, *38*(7), 6072-6084. https://doi.org/10.1021/acs.energyfuels.4c00005

Wulandari, M.P., Fatoni, R., & Widayatno, T. (2024). Production of pyrolysis active carbon based on tuna head bone waste for supercapacitor applications. In *AIP Conference Proceedings* (Vol. 3074, No. 1, p. 040007). AIP Publishing LLC. https://doi.org/10.1063/5.0211290

Yassine, M., & Fabris, D. (2017). Performance of commercially available supercapacitors. *Energies*, *10*(9), 1340. https://doi.org/10.3390/en10091340

Yun, Y.S., Cho, S.Y., Shim, J., Kim, B.H., Chang, S.J., Baek, S.J., Huh, Y.S., Tak, Y., Park, Y.W., Park, S., & Jin, H.J. (2013). Microporous carbon nanoplates from regenerated silk proteins for supercapacitors. *Advanced Materials*, *25*(14), 1993-1998. https://doi.org/10.1002/adma.201204692

Zhang, L., Gonçalves, A.A., & Jaroniec, M. (2023). Synthesis of nanoporous carbonaceous materials at lower temperatures. *Frontiers in Chemistry*, *11*, 1277826. https://doi.org/10.3389/fchem.2023.1277826

Zhao, G., Chen, C., Yu, D., Sun, L., Yang, C., Zhang, H., Sun, Y., Besenbacher, F., & Yu, M. (2018). One-step production of ONS co-doped three-dimensional hierarchical porous carbons for high-performance supercapacitors. *Nano Energy*, *47*, 547-555. https://doi.org/10.1016/j.nanoen.2018.03.016

Zhu, X., Zhang, R., Rong, S., Zhang, L., & Ma, C. (2021). A systematic preparation mechanism for directional regulation of pore structure in activated carbon including specific surface area and pore hierarchy. *Journal of Analytical and Applied Pyrolysis*, *158*, 105266. https://doi.org/10.1016/j.jaap.2021.105266